

Enhanced Non-linear Response by Manipulating the Dirac Point in the (111) LaTiO₃/SrTiO₃ Interface

G. Tuvia,¹ A. Burshtein,¹ I. Silber,¹ A. Aharony,¹ O. Entin-Wohlman,¹ M. Goldstein,¹ and Y. Dagan^{1,*}

¹*School of Physics and Astronomy, Tel-Aviv University, Tel Aviv, 6997801, Israel*

Tunable spin-orbit interaction (SOI) is an important feature for future spin-based devices. In the presence of a magnetic field, SOI induces an asymmetry in the energy bands, which can produce non-linear transport effects ($V \sim I^2$). Here, we focus on such effects to study the role of SOI in the (111) LaTiO₃/SrTiO₃ interface. This system is a convenient platform for understanding the role of SOI since it exhibits a single-band Hall-response through the entire gate-voltage range studied. We report a pronounced rise in the non-linear longitudinal resistance at a critical in-plane field H_{cr} . This rise disappears when a small out-of-plane field component is present. We explain these results by considering the location of the Dirac point formed at the crossing of the spin-split energy bands. An in-plane magnetic field pushes this point outside of the Fermi contour, and consequently changes the symmetry of the Fermi contours and intensifies the non-linear transport. An out-of-plane magnetic field opens a gap at the Dirac point, thereby significantly diminishing the non-linear effects. We propose that magnetoresistance effects previously reported in interfaces with SOI could be comprehended within our suggested scenario.

Rashba-type spin-orbit interaction (SOI) [1] arises in systems lacking inversion symmetry, such as polar semiconductors [2, 3] and interfaces or surfaces [4, 5]. This interaction lifts the spin degeneracy, leading to the splitting of the electronic bands depending on their spin. Such spin-split systems exhibit a multitude of phenomena that hold great promise for spin-based devices [6]. Two-dimensional electron systems are especially interesting in this respect, as the magnitude of their SOI can be tuned by gating [7]. For example, in SrTiO₃ based interfaces, SOI plays a role in phenomena such as weak anti-localization [8], magnetoresistance effects [9], superconductivity [10], and formation of Berry curvature dipoles [11], all of which can be tuned by gate. The (111) surface of SrTiO₃ is particularly intriguing due to its triangular structure, which further reduces the symmetry, leading to rich spin textures [11, 12], and six-fold anisotropic magnetoresistance [13].

Non-linear transport effects ($V \sim I^2$) are useful probes for exploring quantum materials with broken inversion symmetry. The various components of the non-linear tensor contain rich information on a variety of phenomena such as skew scattering [14, 15], superconducting fluctuations [16, 17], and Berry curvature dipoles [11]. Such phenomena may result in pronounced effects in the non-linear transport while being hard to detect in conventional linear measurements.

For systems with SOI, a magnetic field causes the spin-split bands to move in momentum space perpendicular to the magnetic field and the direction in which inversion is broken. This asymmetric band structure can lead to a longitudinal non-linear resistance which is antisymmetric with respect to the magnetic field. This antisymmetric component can lend useful information regarding spin-texture and the band structure of the system. [3, 12, 18–

20].

At the interface between the Mott insulator LaTiO₃ and the band insulator SrTiO₃, the Ti³⁺ and Ti⁴⁺ valences hybridize [21, 22]. For the (001) interface, this region of hybridized Ti valences was shown to result in two-dimensional conductivity [21] and superconductivity [23].

Here we study the electronic properties of the (111) LaTiO₃/SrTiO₃ interface. We focus on the longitudinal antisymmetric term of the non-linear resistivity tensor. We identify a field scale, H_{cr} , beyond which this non-linear component is enhanced. We present a simple model that associates H_{cr} with the field at which a Rashba-Dirac point is excluded from the Fermi contour.

A thin layer of LaTiO₃ is deposited on a (111) SrTiO₃

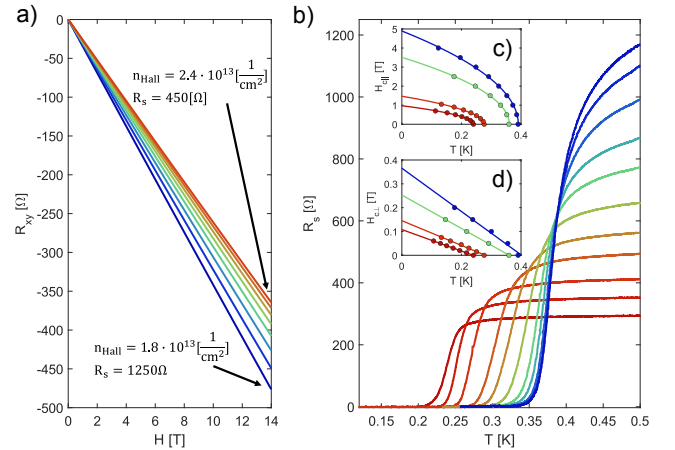


FIG. 1. Hall and superconductivity measurements. (a) Hall effect for various gate-voltages at 10 K, displaying a perfectly linear one-band behavior. (b) Superconducting transitions for various gates-voltages. (c)-(d) In-plane and out-of-plane superconducting critical fields at various temperatures and gates exhibiting a two-dimensional behavior.

* Corresponding author: yodagan@taux.tau.ac.il

substrate by pulsed laser deposition. Devices with current driven along various crystal axes are defined using photolithography (see supplemental material for details[24]). We begin by showing that for all gate voltages studied, the Hall resistance exhibits a linear, single-band-type dependence on the magnetic field with no significant deviations up to 14 T (Fig. 1(a)).

At low temperatures, the interface becomes superconducting (Fig. 1(b)). We find that as the gate-voltage *increases* (higher carrier density and lower sheet resistance), the superconducting transition temperature T_c *decreases*, typical of an “overdoped” regime. Throughout this work, results are plotted as a function of the sheet resistance instead of gate-voltage to account for the dependence of the resistance on the training history of the gate-voltage (see correspondence between the sheet resistance and the carrier density in Fig. S6 [24]).

To demonstrate the two-dimensional nature of superconductivity, we present the in-plane and out-of-plane superconducting critical magnetic fields in Fig. 1(c)-(d), respectively. For all gate-voltages studied, we observe a linear (square root) relation between the out-of-plane (in-plane) superconducting critical field and the temperature as expected for two-dimensional superconductivity. Furthermore, the superconducting coherence length ($\xi = 30\text{--}55$ nm, depending on gate) and the upper bound for the thickness of the superconducting layer ($d = 8\text{--}21$ nm) satisfy $\xi > d$ for all gate-voltages.

To measure the non-linear transport, we apply an alternating current and measure the longitudinal second harmonic voltage drop [3, 12, 19]. We focus on anti-symmetric terms $V_{2\omega}(H) = -V_{2\omega}(-H)$, where H is the magnetic field. It is useful to define $\gamma = \frac{2R_{2\omega}}{R_0 H I}$, where $R_{2\omega} = V_{2\omega}/I$ is the second-harmonic resistance, R_0 is the Ohmic resistance, I is the current, γ is the coefficient of the non-linear term in the resistance:

$$R(I, H) = R_0(1 + \beta H^2 + \gamma IH), \quad (1)$$

and β is the orbital magnetoresistance coefficient.

The second-harmonic resistance of the interface exhibits a pronounced enhancement beyond a critical (in-plane) transverse magnetic field H_{cr} (Fig. 2). For the low-field regime ($H < H_{cr}$), the second-harmonic effect is small and depends linearly on the transverse magnetic field. This behavior is further illustrated in the low-field inset, where γ has a sinusoidal dependence on the in-plane angle ϕ , defined as the angle between the in-plane magnetic field and the current (bottom inset). However, as the magnetic field exceeds the critical magnetic field ($H > H_{cr}$), γ increases substantially and exhibits oscillations depending on ϕ (see high-field inset). As can be seen in the supplemental material Fig. S2 [24], these high-field oscillations depend on the magnitude of the magnetic field and on direction of the current with respect to the crystal axes.

The sharp increase of $R_{2\omega}$ shown in Fig. 2 is extremely sensitive to the application of an out-of-plane magnetic

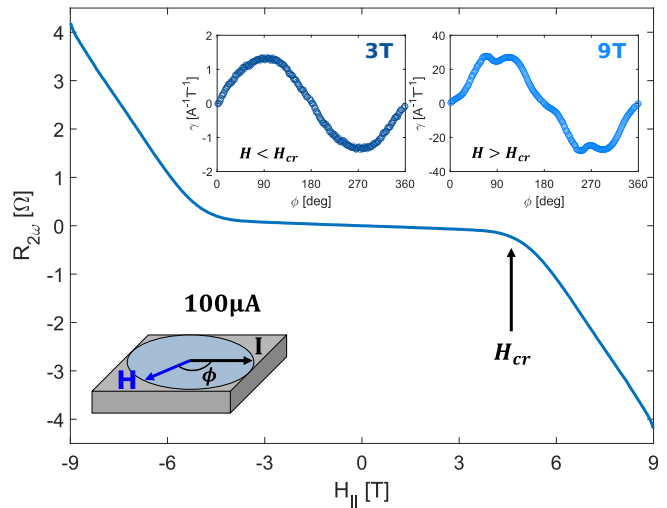


FIG. 2. The second-harmonic resistance versus the in-plane magnetic field at $T=3$ K and $R_s=380$ Ω ; H_{cr} is indicated. Top inset: Dependence of $\gamma = \frac{2R_{2\omega}}{R_0 H I}$ on the in-plane angle ϕ . In the low-field regime, the effect depends only on the component of the field perpendicular to the current. In the high-field regime, the effect also depends on the in-plane field angle ϕ . Bottom inset: Sketch of the sample, current, and magnetic field. In all such sketches throughout this work, the SrTiO_3 is facing up, while the LaTiO_3 is facing down.

field. This can be seen in Fig. 3(a), where a magnetic field of 9 T ($> H_{cr}$) is rotated out of the plane of the interface, perpendicular to the current (see top image in Fig. 3(e) for clarity). γ rapidly decays with the introduction of a small out-of-plane contribution. Conversely, Fig. 3(b) shows the low-field behavior ($H < H_{cr}$), where γ is much smaller, and depends linearly on the in-plane magnetic field component. Note that the $V \sim I^2$ dependence of the main non-linear effects studied in this work is confirmed in the supplemental material [24], where we present current-dependant second harmonic measurements (Fig. S9) and direct-current versus voltage measurements (Fig. S10) under magnetic fields.

To further investigate the influence of out-of-plane magnetic fields, a constant in-plane field of 7.8 T ($> H_{cr}$) was rotated while applying various out-of-plane fields (see bottom panel of Fig. 3(e)). Fig. 3(c) presents the results for out-of-plane fields of +4.5 T (red), -4.5 T (black), and 0 T (blue). Although $H > H_{cr}$ in these measurements, the signal with an out-of-plane contribution resembles the behavior observed in the low-field regime, suggesting that an out-of-plane magnetic field mostly counteracts the high field enhancement of γ .

The same magnetic field measurement scheme used in Fig. 3(c) was employed while measuring the first-harmonic sheet resistance R_s (see Fig. 3(d)). The measurements performed with no out-of-plane field (blue curve) primarily exhibit a two-fold effect as a function of ϕ , accompanied by four-fold and six-fold contributions (see Fig. S4 [24]), similar to those previously re-

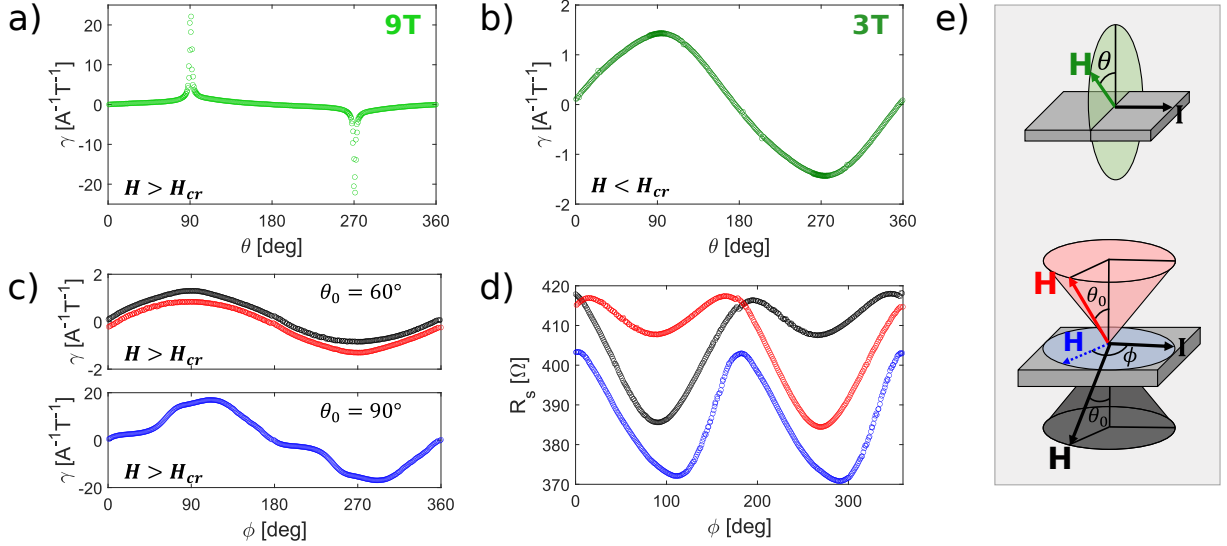


FIG. 3. Effects of the out-of-plane magnetic field. (a,b) γ is shown as a function of the out-of-plane magnetic field angle θ for total field magnitudes of 9 T (a) and 3 T (b). A sharp increase in γ is observed for the high field regime when the magnetic field is in-plane. (c) γ is shown versus the in-plane angle ϕ for $H_{\parallel} = 7.8$ T and $H_{\perp} = 4.5$ T (red), -4.5 T (black), and 0 T (blue). (d) Similar magnetic field scheme like (c) for the first-harmonic measurements. Note the mirror symmetry breaking for the red and black curves. (e) Sketch of the magnetic field configurations employed in the measurements presented in this figure. Temperatures and sheet resistances for these figures slightly vary due to different cool-downs: (a) $T = 3$ K and $R_s = 380$ Ω , (b) $T = 1.8$ K and $R_s = 412$ Ω , (c)-(d) $T = 1.9$ K and $R_s = 407$ Ω .

ported for the (111) $\text{LaAlO}_3/\text{SrTiO}_3$ interface [13]. However, upon the introduction of an out-of-plane magnetic field (red/black curves), an unusual anisotropy emerges. This anisotropic component breaks the mirror symmetry of the magnetic field with respect to the interface, $R(H_{\parallel}, H_{\perp}) \neq R(H_{\parallel}, -H_{\perp})$. Interestingly, for a particular in-plane angle, this mirror symmetry is preserved. This angle (defined as ϕ_0) exhibits a three-fold dependence on the crystal axis along which current is driven (as seen in Fig. S3 [24]). While the understanding of this effect lies beyond the scope of this work, its three-fold nature and dependence on the out-of-plane magnetic field suggests that it is a consequence of the three-fold out-of-plane tilt of the spin texture observed for the surface of (111) SrTiO_3 [12].

The high-field enhancement of $R_{2\omega}$ decays with temperature, almost vanishing at ≈ 10 K. This behavior can be observed in Fig. 4(a), where a transverse magnetic field is applied at various temperatures. To quantify the effect of temperature, the γ factor at 9 T is plotted in Fig. 4(b) for various temperatures after subtracting the small low-field contribution, extrapolated to 9 T (the result is defined as $\Delta\gamma$). As shown in Fig. S5 (b) [24], the critical field H_{cr} does not change within this temperature range. A similar analysis was performed as a function of gate-voltage and is shown in Fig. 4(c)-(d). A strong decay of the effect is observed as the gate-voltage becomes more negative. In contrast to the effect of temperature, the critical field H_{cr} changes with the gate-voltage (see Fig. S5 (a) [24]), reflecting a change of the chemical potential

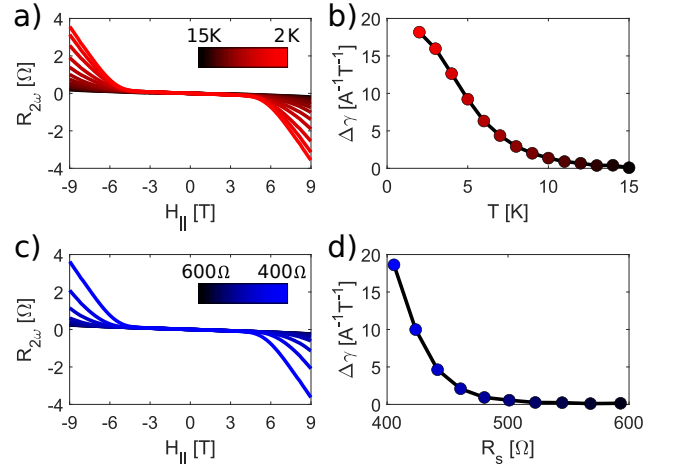


FIG. 4. (a) Second-harmonic resistance versus transverse magnetic field at different temperatures. (b) γ at 9 T after subtracting the low-field contribution, versus temperature. (c,d) Similar to (a,b) but as a function of gate-voltage represented by the sheet resistance (R_s). The effect quickly decays at more negative gates-voltages (higher resistances). Temperature-dependent measurements were conducted for the lowest R_s , gate-dependent measurements were conducted at 2 K.

and the SOI magnitude.

To elucidate the critical behavior observed in the second-harmonic transport, we propose a minimal model that can capture the essential features observed in exper-

iment. Our model assumes a two-dimensional electron system with a simple parabolic dispersion and a Rashba-type SOI in the presence of a Zeeman magnetic field:

$$\mathcal{H} = \frac{k^2}{2m} + \lambda(k_x\sigma_y - k_y\sigma_x) - B_y\sigma_y - B_z\sigma_z, \quad (2)$$

where λ represents the magnitude of the SOI, $k_{x/y}$ denote the momentum components which are parallel/perpendicular to the current, $\sigma_{x/y/z}$ are the Pauli matrices, and B_y/B_z are the transverse/out-of-plane magnetic field components. Throughout this work, B is used for magnetic fields in the calculations in units of energy assuming $g=2$, while H is used for the magnetic fields applied in the experiment. Note that we assume that only a single electronic band is occupied. In the supplemental material [24], we address a scenario where a second electronic band is occupied, but is very dilute so its effect is unnoticeable in the Hall effect presented in Fig. 1 (a). We show that such a second-band with reasonable physical parameters cannot account for our experimental observations.

Previous calculations by Ideue *et al.* [3] have shown that for such a system, the geometry of the Fermi contour changes at critical values of the magnetic field or chemical potential, leading to a change in γ . To map this scenario onto the (111) LaTiO₃/SrTiO₃ interface studied here, we estimate the relevant parameters of the system. The spin-orbit energy of SrTiO₃ based interfaces is estimated at a few meV [9–11] while the electron density of a few $10^{13}[\frac{1}{\text{cm}^2}]$ results in a chemical potential of roughly 100meV. To ensure that the estimation of the spin-orbit energy is reasonable, we perform standard magnetoresistance measurements at low temperatures (Fig. S6 [24]). The relatively small spin-splitting effect means that, for $B = 0$, the spin-split energy bands cross at a single point below the Fermi energy. This crossing point is coined as “the Dirac point” due to the linear dispersion in its vicinity. Once a transverse magnetic field B_y is applied, the energy of the Dirac point increases, reaching the Fermi energy at the critical field $B_{cr} = \sqrt{2m\lambda^2\mu}$. Within the relevant parameter regime, the calculated B_{cr} falls reasonably close to the critical field observed in experiment.

As we now show, the exclusion of the Dirac point from the Fermi contour leads to a dramatic increase in $R_{2\omega}$, similar to our experimental observation. The second-harmonic resistance is proportional to σ_2/σ_1^2 , where $J^{(i)} = \sigma_i E^i$. By expanding the Boltzmann equation to a second order in the electric field within the single relaxation time approximation [24], we obtain the second order current:

$$J^{(2)} = -e^3\tau^2 E^2 \sum_{r=\pm} \int \frac{dk_x dk_y}{(2\pi)^2} \frac{\partial^3 \varepsilon_k^r}{\partial k_x^3} f_0^r, \quad (3)$$

where τ is the scattering time, E is the electric field applied in the \hat{x} direction, f_0^\pm are the Fermi-Dirac distributions of the bands, and ε_k^r are the corresponding energies.

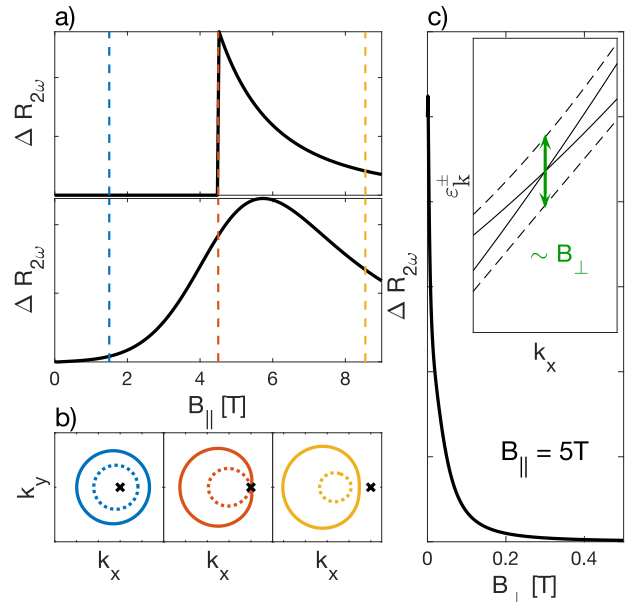


FIG. 5. Minimal model calculations. (a) Calculated second-harmonic resistance as function of transverse magnetic field with no out-of-plane field (top panel) and a small out-of-plane field (bottom panel). (b) Fermi contours for $B_{||} < B_{cr}$, $B_{||} = B_{cr}$, $B_{||} > B_{cr}$. For every scenario, the location of the Dirac point is marked. (c) Second-harmonic resistance vs. the perpendicular magnetic field with constant high transverse magnetic field. Inset: Illustration of band gap opening with perpendicular magnetic field.

Considering first the case of $B_z = 0$, the energy bands are given by:

$$\varepsilon_k^\pm = \frac{k^2}{2m} \pm \sqrt{(\lambda k_x - B_y)^2 + \lambda^2 k_y^2}. \quad (4)$$

While the third derivative of the parabolic term $k^2/2m$ in Eq. (4) vanishes, the Dirac point acts as a source for higher derivatives, and yields a non-vanishing contribution to the integrands in Eq. (3). In section 1 of the supplemental material [24] we show that for $B_y < B_{cr}$, the sum of third derivatives of the bands is antisymmetric under a π rotation around the Dirac point, such that $J^{(2)} = 0$. This symmetry is broken for $B_y > B_{cr}$, where the Dirac point is excluded from both Fermi contours, and $J^{(2)}$ assumes a finite value. Utilizing the above expressions, we calculate $R_{2\omega}$ as function of B_y . The result, presented in the top panel of Fig. 5(a), shows that the second harmonic signal is zero for low fields ($B_y < B_{cr}$), significantly increases once the Fermi contours intersect at $B_y = B_{cr}$, and finally decreases for $B_y > B_{cr}$. The position of this Dirac point with respect to the Fermi contours is illustrated in Fig. 5(b) for several values of the transverse magnetic field. We note that the spin-texture of the Fermi contours also changes at the critical field — for the low-field regime, the spin texture completes a 2π rotation when going along the Fermi contours

while it does not above the critical field [24]. While this Dirac point mechanism can explain the critical magnetic field observed in experiment, the strong decay of γ with temperature and gate-voltage shown in Fig. 4(b), (d) requires an analysis beyond the single relaxation time approximation used here [24].

The presence of an energy gap between the spin-split bands can significantly change the ideal result presented in Fig. 5(a) (top panel). In the bottom panel of Fig. 5(a), we show the calculated $R_{2\omega}$ as a function of the transverse magnetic field B_y when a small gap is opened by a perpendicular magnetic field, equivalent to $B_z = 10$ mT. This gap adds a new asymmetry to the energy bands, leading to a small non-zero coefficient below the critical field and a much more gradual increase of $R_{2\omega}$ at the critical field. In Fig. 5(c), we show the calculated $R_{2\omega}$ in a constant transverse magnetic field ($B_y > B_{cr}$) while a perpendicular magnetic field B_z is applied. The second-harmonic signal quickly decays, similar to the experimental result shown in Fig. 3. This decay reflects the fact that the gap smears-out the Dirac point, as seen in Fig. 5(c), which substantially decreases the magnitude of the third derivative.

It is interesting to compare the (111) LaTiO₃/SrTiO₃ interface studied here to the more extensively studied LaAlO₃/SrTiO₃ interface. While for both (001) and (111) LaAlO₃/SrTiO₃ interfaces, the overdoped regime of superconductivity is accompanied by a clear two-band Hall signal [25–27]. Similarly, certain magneto-transport effects, such as the anomalous Hall effect induced by an in-plane magnetic field [9, 28], and anisotropic magnetoresistance [13, 28], manifest in LaAlO₃/SrTiO₃ interfaces only when a two-band Hall behavior is present. Nevertheless, in the case of the studied interface, these phenomena are observed with a single occupied energy band (refer to Fig. 1 for overdoped superconductivity, Fig. S8 for in-plane anomalous Hall, and Fig. S4 for magnetoresistance measurements [24]). This distinction warrants further exploration in future research. It is important to note that, within the context of this study, these magneto-transport effects are evident at low temperatures, high gate voltages, and under the influence of a strong in-plane magnetic field, conditions associated with a large γ . As noted in previous works [25–27], the

Rashba SOI only adds a small correction to the band structure. However, as we show in this work, the manipulation of the SO induced Dirac point changes the symmetry of the energy bands, which has a substantial effect on the non-linear transport, and possibly also the linear magneto-transport.

In summary, we measure the new (111) LaTiO₃/SrTiO₃ interface. We observe superconductivity in this interface along with one-band-type Hall-signal. This behavior is observed even when T_c is decreased upon adding charge carriers (overdoped regime), in contrast to the well studied LaAlO₃/SrTiO₃ interfaces. Our main finding is a sharp increase of the magnitude of the non-linear transport of the (111) LaTiO₃/SrTiO₃ interface at a critical magnetic field H_{cr} . By employing a minimal model incorporating SOI at a generic interface, we show that H_{cr} can be understood as the field at which the spin-orbit-induced Dirac point is excluded from the Fermi contour. According to our model, beyond this field, the symmetry and the spin-texture of the Fermi contours change simultaneously. We further show that a minuscule out-of-plane magnetic field opens a gap between the spin-split bands, which significantly reduces the second-harmonic effect, as observed in our experiment. We suggest that this mechanism sheds light on some of the unusual magneto-transport effects observed in previous experiments on oxide interfaces.

Acknowledgements

We thank Tobias Holder, Roni Ilan, and Shay Sandik for useful discussions. Asaf Yagoda and Elad Mileikowsky assisted with the transport setup. This work was partially supported (Y.D.) By the Israeli Science Foundation under grant 476/22 and by the PAZI foundation under grant 326-1/20. M.G. was supported by the Israel Science Foundation (ISF) and the Directorate for Defense Research and Development (DDR&D) Grant No. 3427/21, and by the US-Israel Binational Science Foundation (BSF) Grant No. 2020072. A.B. is supported by the Adams Fellowship Program of the Israel Academy of Sciences and Humanities.

-
- [1] E. Rashba, *Sov. Phys.-Solid State* **2**, 1109 (1960).
 - [2] K. Ishizaka, M. S. Bahramy, H. Murakawa, M. Sakano, T. Shimojima, T. Sonobe, K. Koizumi, S. Shin, H. Miyahara, A. Kimura, K. Miyamoto, T. Okuda, H. Namatame, M. Taniguchi, R. Arita, N. Nagaosa, K. Kobayashi, Y. Murakami, R. Kumai, Y. Kaneko, Y. Onose, and Y. Tokura, *Nature Materials* **10**, 521 (2011).
 - [3] T. Ideue, K. Hamamoto, S. Koshikawa, M. Ezawa, S. Shimizu, Y. Kaneko, Y. Tokura, N. Nagaosa, and Y. Iwasa, *Nature Physics* **13**, 578 (2017).
 - [4] A. F. Santander-Syro, F. Fortuna, C. Bareille, T. C. Rödel, G. Landolt, N. C. Plumb, J. H. Dil, and M. Radović, *Nature Materials* **13**, 1085 (2014).
 - [5] S. LaShell, B. A. McDougall, and E. Jensen, *Phys. Rev. Lett.* **77**, 3419 (1996).
 - [6] A. Manchon, H. C. Koo, J. Nitta, S. M. Frolov, and R. A. Duine, *Nature Materials* **14**, 871 (2015).
 - [7] K. Premasiri and X. P. Gao, *Journal of Physics: Condensed Matter* **31**, 193001 (2019).
 - [8] D. Rakhmilevitch, M. Ben Shalom, M. Eshkol, A. Tsukernik, A. Palevski, and Y. Dagan, *Phys. Rev. B* **82**,

- 235119 (2010).
- [9] M. Ben Shalom, M. Sachs, D. Rakhmilevitch, A. Palevski, and Y. Dagan, *Phys. Rev. Lett.* **104**, 126802 (2010).
- [10] P. K. Rout, E. Maniv, and Y. Dagan, *Phys. Rev. Lett.* **119**, 237002 (2017).
- [11] E. Lesne, Y. G. Sağlam, R. Battilomo, M. T. Mercaldo, T. C. van Thiel, U. Filippozzi, C. Noce, M. Cuoco, G. A. Steele, C. Ortix, and A. D. Caviglia, *Nature Materials* **22**, 576 (2023).
- [12] P. He, S. M. Walker, S. S.-L. Zhang, F. Y. Bruno, M. S. Bahramy, J. M. Lee, R. Ramaswamy, K. Cai, O. Heinonen, G. Vignale, F. Baumberger, and H. Yang, *Phys. Rev. Lett.* **120**, 266802 (2018).
- [13] P. K. Rout, I. Agireen, E. Maniv, M. Goldstein, and Y. Dagan, *Phys. Rev. B* **95**, 241107 (2017).
- [14] H. Isobe, S.-Y. Xu, and L. Fu, *Science Advances* **6**, eaay2497 (2020).
- [15] P. He, H. Isobe, D. Zhu, C.-H. Hsu, L. Fu, and H. Yang, *Nature Communications* **12**, 698 (2021).
- [16] Y. M. Itahashi, T. Ideue, Y. Saito, S. Shimizu, T. Ouchi, T. Nojima, and Y. Iwasa, *Science Advances* **6**, eaay9120 (2020).
- [17] Y. M. Itahashi, T. Ideue, S. Hoshino, C. Goto, H. Namiki, T. Sasagawa, and Y. Iwasa, *Nature Communications* **13**, 1659 (2022).
- [18] P. He, C.-H. Hsu, S. Shi, K. Cai, J. Wang, Q. Wang, G. Eda, H. Lin, V. M. Pereira, and H. Yang, *Nature Communications* **10**, 1290 (2019).
- [19] D. Choe, M.-J. Jin, S.-I. Kim, H.-J. Choi, J. Jo, I. Oh, J. Park, H. Jin, H. C. Koo, B.-C. Min, S. Hong, H.-W. Lee, S.-H. Baek, and J.-W. Yoo, *Nature Communications* **10**, 4510 (2019).
- [20] Y. Li, Y. Li, P. Li, B. Fang, X. Yang, Y. Wen, D.-x. Zheng, C.-h. Zhang, X. He, A. Manchon, Z.-H. Cheng, and X.-x. Zhang, *Nature Communications* **12**, 540 (2021).
- [21] A. Ohtomo, D. A. Muller, J. L. Grazul, and H. Y. Hwang, *Nature* **419**, 378 (2002).
- [22] Y. Wang, Y. Liang, M. Meng, Q. An, B. Ge, M. Liu, F. Yang, and J. Guo, *Journal of Applied Physics* **128**, 035301 (2020).
- [23] J. Biscaras, N. Bergeal, A. Kushwaha, T. Wolf, A. Rastogi, R. C. Budhani, and J. Lesueur, *Nature Communications* **1**, 89 (2010).
- [24] See Supplemental Material below.
- [25] A. Joshua, S. Pecker, J. Ruhman, E. Altman, and S. Ilani, *Nature Communications* **3**, 1129 (2012).
- [26] E. Maniv, M. B. Shalom, A. Ron, M. Mograbi, A. Palevski, M. Goldstein, and Y. Dagan, *Nature Communications* **6**, 8239 (2015).
- [27] U. Khanna, P. K. Rout, M. Mograbi, G. Tuvia, I. Leermakers, U. Zeitler, Y. Dagan, and M. Goldstein, *Phys. Rev. Lett.* **123**, 036805 (2019).
- [28] A. Joshua, J. Ruhman, S. Pecker, E. Altman, and S. Ilani, *Proceedings of the National Academy of Sciences* **110**, 9633 (2013).

Supplementary - Enhanced Non-linear Response by Manipulating the Dirac Point in the (111) $\text{LaTiO}_3/\text{SrTiO}_3$ Interface

G. Tuvia,¹ A. Burshtein,¹ I. Silber,¹ A. Aharony,¹ O. Entin-Wohlman,¹ M. Goldstein,¹ and Y. Dagan^{1,*}

¹*School of Physics and Astronomy, Tel-Aviv University, Tel Aviv, 6997801, Israel*

arXiv:2309.07706v2 [cond-mat.str-el] 22 Oct 2024

* Corresponding author: yodagan@tauex.tau.ac.il

I. SUPPLEMENTARY SECTION 1 — BOLTZMANN-EQUATION CALCULATIONS

A. Hamiltonian and energy bands

We consider a 2D Hamiltonian with a parabolic dispersion relation, an external magnetic field, and a Rashba spin-orbit interaction term,

$$\mathcal{H} = \frac{k^2}{2m} + \lambda(k_x\sigma_y - k_y\sigma_x) - B_x\sigma_x - B_y\sigma_y - B_z\sigma_z, \quad (\text{S1})$$

where $k_{x,y}$ denote the momentum components, λ is the spin-orbit coupling coefficient (in momentum units), $B_{x,y,z}$ are the components of the magnetic field (in energy units), $\sigma_{x,y,z}$ are the Pauli matrices, and m is the effective mass of the electrons. Here we consider only the Zeeman field and neglect the orbital effect of the magnetic field. The energy bands are given by

$$\varepsilon^\pm(k) = \frac{k^2}{2m} \pm \sqrt{(\lambda k_x - B_y)^2 + (\lambda k_y + B_x)^2 + B_z^2}. \quad (\text{S2})$$

It is more convenient to redefine the momentum as $p_x = k_x - \frac{B_y}{\lambda}$ and $p_y = k_y + \frac{B_x}{\lambda}$, so that the minimum distance between the bands is at the origin, $p = 0$ (where $p^2 = p_x^2 + p_y^2$):

$$\varepsilon^\pm(p) = \frac{p^2}{2m} - \frac{pB_\parallel \sin(\theta - \varphi)}{m\lambda} + \frac{B_\parallel^2}{2m\lambda^2} \pm \sqrt{\lambda^2 p^2 + B_z^2}, \quad (\text{S3})$$

where $B_x = B_\parallel \cos \varphi$, $B_y = B_\parallel \sin \varphi$ are the components of the in-plane magnetic field, and $p_x = p \cos \theta$, $p_y = p \sin \theta$ are the components of the momentum. In the absence of an out-of-plane magnetic field, the bands intersect at the origin; a gap is opened for $B_z \neq 0$. The corresponding eigenvectors are spin-polarized,

$$\psi^\pm(\theta) = \frac{1}{\sqrt{2}} \begin{pmatrix} 1 \\ \pm i \text{sign}(\lambda) e^{i\theta} \end{pmatrix}. \quad (\text{S4})$$

The Fermi momenta $p_\pm^\pm(\theta)$ are the solutions to $\mu = \varepsilon^\pm(p_\pm^\pm(\theta))$, where μ is the chemical potential. At $B_z = 0$, an analytical solution is obtained,

$$p_r^\pm(\theta) = \frac{B_\parallel}{\lambda} \sin(\theta - \varphi) - r |\lambda| m \pm \sqrt{2m\tilde{\mu} - \frac{B_\parallel^2}{\lambda^2} \cos^2(\theta - \varphi) - 2r \text{sign}(\lambda) m B_\parallel \sin(\theta - \varphi)}, \quad (\text{S5})$$

where $r = \pm$ labels the bands, and $\tilde{\mu} = \mu + m\lambda^2/2$ is the chemical potential measured with respect to the bottom of the lower band at $B_\parallel = 0$. The momenta $p_r^-(\theta)$ and $p_r^+(\theta)$ constitute the inner and outer Fermi contours of the r band, and are defined only for angles θ for which $p_r^\pm(\theta) \in \mathbb{R}^+$. The critical field, $B_{cr} = \sqrt{2m\lambda^2\mu}$, determines whether or not the origin $p = 0$ is included in the Fermi contour, as demonstrated in Fig. 5 in the main text. Namely, for $B_\parallel < B_{cr}$, one finds that $p_\pm^-(\theta) < 0$ and $p_\pm^+(\theta) \in \mathbb{R}^+$ for any θ , so $p = 0$ is included in the Fermi contour of both bands. For $B_\parallel > B_{cr}$, there are angles where the Fermi momenta are undefined, such that $p = 0$ is excluded from the Fermi contour of the bands. We assume throughout that $m\lambda^2 \ll B_{cr}, \mu$, and also that $B_\parallel \ll \mu$, such that both bands are occupied for the parameters used in the experiment. As mentioned in the main text, typical values of λ and μ in the LaTiO₃/SrTiO₃ interface yield critical fields on the order of a few Tesla, within the experimental range of applied magnetic fields.

B. Calculation of the first and second harmonic currents

We follow the method used in Ref. [1] for calculating the second-harmonic resistance. We begin by writing down the Boltzmann equation for the distribution functions of the bands, $f^\pm(\vec{E}, \mu, \vec{p})$, for an electric field applied in the \hat{x} direction, $\vec{E} = E\hat{x}$. Within the relaxation-time approximation, one finds

$$-e\vec{E} \cdot \vec{\nabla}_p f^\pm = -eE \frac{\partial f^\pm}{\partial p_x} = -\frac{1}{\tau} (f^\pm - f_0^\pm), \quad (\text{S6})$$

where $f_0^\pm = 1 / (\exp \{ (\varepsilon_p^\pm - \mu) / k_B T \} + 1)$ is the Fermi-Dirac distribution function, and τ is the scattering time. Expanding f^\pm as a power series in the electric field E , $f^\pm = f_0^\pm + f_1^\pm + f_2^\pm + \dots$, with $f_n^\pm \sim E^n$, we find

$$-eE \frac{\partial}{\partial p_x} \sum_{n=0}^{\infty} f_n^\pm = -\frac{1}{\tau} \sum_{n=1}^{\infty} f_n^\pm. \quad (\text{S7})$$

Equating the coefficients of the electric field term-by-term yields

$$f_n^\pm = eE\tau \frac{\partial f_{n-1}^\pm}{\partial p_x}. \quad (\text{S8})$$

We may then find the current from the distribution functions. The n -th harmonic contribution to the current is given by

$$\begin{aligned} J^{(n)} &= \sum_{r=\pm} \int \frac{dp_x dp_y}{(2\pi)^2} \left(-e \frac{\partial \varepsilon_p^r}{\partial p_x} \right) f_n^r \\ &= (-1)^{n+1} e (e\tau E)^n \sum_{r=\pm} \int \frac{dp_x dp_y}{(2\pi)^2} \frac{\partial^{n+1} \varepsilon_p^r}{\partial p_x^{n+1}} f_0^r. \end{aligned} \quad (\text{S9})$$

The first and second harmonics are given by

$$\begin{aligned} J^{(1)} &= \frac{e^2 \lambda^2 \tau E}{(2\pi)^2} \int dp d\theta \left(\frac{p}{m\lambda^2} (f_0^+ + f_0^-) + \frac{\lambda^2 p^3 \sin^2 \theta + p B_z^2}{(\lambda^2 p^2 + B_z^2)^{3/2}} (f_0^+ - f_0^-) \right), \\ J^{(2)} &= \frac{3e^3 \lambda^4 \tau^2 E^2}{(2\pi)^2} \int dp d\theta \frac{\lambda^2 p^4 \cos \theta \sin^2 \theta + B_z^2 p^2 \cos \theta}{(\lambda^2 p^2 + B_z^2)^{5/2}} (f_0^+ - f_0^-). \end{aligned} \quad (\text{S10})$$

Note that the dependence on B_{\parallel} is encoded in the Fermi-Dirac distribution functions. The n -th harmonic conductance is defined by $\sigma_n = E^n / J^{(n)}$; the second-harmonic resistance is given by $R_{2\omega} \sim \sigma_2 / \sigma_1^2$, and is independent of the scattering time τ .

The double integrals may be evaluated numerically for any value of B_{\parallel}, B_z at any temperature. To gain analytical insight, consider the case $B_z = 0$ and $T = 0$. The Fermi-Dirac distributions become step functions, and the integrals over p may be easily evaluated analytically. Below the critical field, $B_{\parallel} < B_{cr}$, one finds from Eq. (S5) that $p_r^-(\theta) < 0$ and $p_r^+(\theta) > 0$ for all θ , leading to

$$\begin{aligned} J^{(1)}(B_{\parallel} < B_{cr}) &= \frac{e^2 \tau E}{(2\pi)^2} \int_0^{2\pi} d\theta \left(\frac{(p_+^+(\theta))^2 + (p_-^+(\theta))^2}{2m} + |\lambda| (p_+^+(\theta) - p_-^+(\theta)) \sin^2 \theta \right), \\ J^{(2)}(B_{\parallel} < B_{cr}) &= \frac{3e^3 |\lambda| \tau^2 E^2}{(2\pi)^2} \int_0^{2\pi} d\theta \log \left(\frac{p_+^+(\theta)}{p_-^+(\theta)} \right) \cos \theta \sin^2 \theta. \end{aligned} \quad (\text{S11})$$

Above the critical field, there are angles θ for which the Fermi momenta are either imaginary or negative. The p integrals may be evaluated as before, but the θ integral is restricted to angles for which $p_{\pm}^{\pm}(\theta) \in \mathbb{R}^+$:

$$\begin{aligned} J^{(1)}(B_{\parallel} > B_{cr}) &= \frac{e^2 \tau E}{(2\pi)^2} \int_{p_{\pm}^{\pm}(\theta) \in \mathbb{R}^+} d\theta \\ &\times \left(\frac{(p_+^+(\theta))^2 + (p_-^+(\theta))^2 - (p_+^-(\theta))^2 - (p_-^-(\theta))^2}{2m} + |\lambda| (p_-^+(\theta) - p_+^+(\theta) + p_+^-(\theta) - p_-^-(\theta)) \sin^2 \theta \right), \\ J^{(2)}(B_{\parallel} > B_{cr}) &= \frac{3e^3 |\lambda| \tau^2 E^2}{(2\pi)^2} \int_{p_{\pm}^{\pm}(\theta) \in \mathbb{R}^+} d\theta \log \left(\frac{p_+^+(\theta) p_-^-(\theta)}{p_-^+(\theta) p_+^-(\theta)} \right) \cos \theta \sin^2 \theta. \end{aligned} \quad (\text{S12})$$

For the first harmonic current, one finds $J^{(1)} = e^2 \tau m / \pi \times (m\lambda^2 + \mu)$ at any $B_{\parallel} < B_y$, and a very small and continuous deviation from this value at $B_{\parallel} > B_y$. Next, consider the integrand of $J^{(2)}$. Using Eq. (S5), we find that the ratio $p_+^{\xi}(\theta) / p_-^{\xi}(\theta)$, for both $\xi = \pm$, is symmetric under the transformation $\theta \rightarrow \theta + \pi$ [1], implying that the integrand

of $J^{(2)}$ above is antisymmetric under such a transformation. Hence, if the origin is included in Fermi contour, so that the integral of $J^{(2)}$ runs over $0 \leq \theta < 2\pi$, one finds $J^{(2)} = 0$. If, however, $B_{\parallel} > B_{cr}$, such that the origin is excluded from the Fermi contour, the integral of $J^{(2)}$ is restricted to a smaller subset of angles θ ; in particular, there are angles θ that are included in the integration regime for which $\theta + \pi$ is excluded from the integral. Hence, above the critical field, the second harmonic current no longer vanishes. At the critical field, $B_{\parallel} = B_{cr}$, the derivative of ε_p^{\pm} with respect to p_x is not continuous; this explains the jump in the second harmonic current, which is determined by the third-order derivative $\partial^3 \varepsilon_p^{\pm} / \partial p_x^3$ [see Eq. (S9)].

As B_{\parallel} is increased beyond the critical field, we expect $J^{(2)}$ to decrease. Let us show this for $B_x = 0$ ($\varphi = \pi/2$). Expanding the logarithm in the $J^{(2)}$ integral in Eq. (S12) for $B_{\parallel} = B_y \gg B_{cr}$, one finds

$$\log \left(\frac{p_+^+(\theta) p_-^-(\theta)}{p_-^+(\theta) p_+^-(\theta)} \right) \approx \frac{4m\lambda^2}{B_y^2} \sqrt{2m\lambda^2 \tilde{\mu} - B_y^2 \sin^2 \theta}. \quad (\text{S13})$$

Plugging into the integral yields

$$\begin{aligned} J^{(2)}(B_y \gg B_{cr}) &\approx \frac{3|\lambda| e^3 \tau^2 E^2}{(2\pi)^2} \frac{4m\lambda^2}{B_y^2} \int_{\sin^2 \theta < \frac{2m\lambda^2 \tilde{\mu}}{B_y^2}, \frac{B_y}{\lambda} \cos \theta < 0} d\theta \sin^2 \theta \cos \theta \sqrt{2m\lambda^2 \tilde{\mu} - B_y^2 \sin^2 \theta} \\ &= \frac{3\pi |\lambda| e^3 \tau^2 E^2}{2(2\pi)^2} \frac{m\lambda^2}{B_y} \left(\frac{B_{cr}}{B_y} \right)^2. \end{aligned} \quad (\text{S14})$$

This shows that the second-harmonic current decreases as B_{\parallel} is increased far beyond the critical field.

C. Perpendicular magnetic field and the role of a gap

The presence of an out-of-plane field B_z introduces two major differences. First, the antisymmetry of the integrand in Eq. (S10) is broken, so that $J^{(2)} \neq 0$ also for $B_{\parallel} < B_{cr}$. Second, B_z opens a gap (as demonstrated in Fig. 5 of the main text), so that the derivatives of the dispersion relation with respect to p_x become continuous, leading to the suppression of the jump at $B_{\parallel} = B_{cr}$. We stress that such features should be generic; there are many different terms that could be added to the Hamiltonian which would break the antisymmetry of the $J^{(2)}$ integrand or open a gap and suppress the jump at $B_{\parallel} = B_{cr}$. We demonstrate this point by adding a cubic ‘‘warping’’ spin-orbit term to the Hamiltonian in Eq. (S1):

$$\mathcal{H}_{\zeta} = \frac{\zeta}{2} (k_+^3 + k_-^3) \sigma_z, \quad (\text{S15})$$

with $k_{\pm} = k_x \pm ik_y$. The energy bands are readily given by

$$\varepsilon_p^{\pm} = \frac{p^2}{2m} - \frac{pB_{\parallel} \sin(\theta - \varphi)}{m\lambda} + \frac{B_{\parallel}^2}{2m\lambda^2} \pm \sqrt{\lambda^2 p^2 + \left(\zeta \left(p \cos \theta + \frac{B_y}{\lambda} \right) \left[\left(p \cos \theta + \frac{B_y}{\lambda} \right)^2 - 3 \left(p \sin \theta - \frac{B_x}{\lambda} \right)^2 \right] - B_z \right)^2}. \quad (\text{S16})$$

Note that, even in the absence of an out-of-plane field B_z , a gap opens if $\zeta \neq 0$, and the bands do not intersect at $p = 0$. The double integrals in Eq. (S9) may be evaluated numerically, revealing a linear growth of $J^{(2)}$ in B_y for $B_y \ll B_{cr}$.

D. Berry curvature and spin texture

The Hamiltonian in Eq. (S1) may be written as $\mathcal{H} = k^2/2m + \mathbf{d} \cdot \boldsymbol{\sigma}$, with $\mathbf{d} = (-\lambda k_y - B_x, \lambda k_x - B_y, -B_z)$. The crossing point at $(k_x, k_y) = (B_y/\lambda, -B_x/\lambda)$ ($p = 0$) is a Dirac point, whose corresponding Dirac cone is titled by the parabolic dispersion relation, as demonstrated in Fig. S1. Its associated Berry curvature is given by $\Omega^{\pm} = \pm \hat{\mathbf{d}} \cdot (\partial_{k_x} \hat{\mathbf{d}} \times \partial_{k_y} \hat{\mathbf{d}}) / 2 = \pm \lambda^2 B_z / |\mathbf{d}|^3$, where + and – correspond to the two energy bands. In the limit of vanishing perpendicular field B_z , the curvature is given by a delta function at the p origin, $\Omega^{\pm} = \pm \pi \delta^{(2)}(p)$. When the in-plane magnetic field is below the critical field, $B_{\parallel} < B_{cr}$, the Dirac point is enclosed by the Fermi contours of both

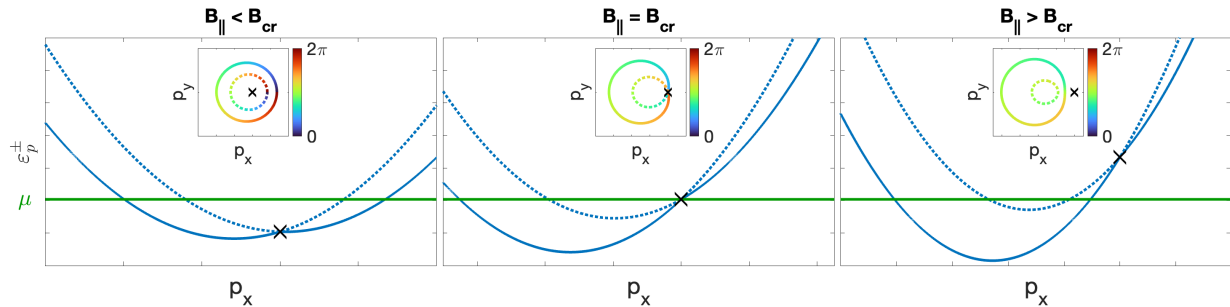


FIG. S1. Energy bands ε_p^- and ε_p^+ , plotted in solid and dotted lines, respectively, as a function of p_x and at $p_y = 0$, for transverse magnetic fields below, at, and above the critical field. The Dirac point at $p = 0$ is marked by an “x” in all figures. The insets show the angle of the spins along the Fermi contours; the spins complete a full 2π rotation for $B_{\parallel} < B_{cr}$ in both bands, but do not complete a full rotation for $B_{\parallel} > B_{cr}$.

bands, and the associated Berry phases of the spin-polarized eigenstates (given in Eq. (S4)) are $\gamma_p^{\pm} = \pm\pi$, such that $\gamma_p^+ + \gamma_p^- = 0$.

It is important to note that while the Berry curvature affects the semi-classical equations of motion, its contribution to the longitudinal second-harmonic current vanishes, as shown in Ref. [2]. Nevertheless, the sharp jump of the second-harmonic resistance occurs just as the Dirac point moves out of both Fermi contours, as demonstrated in Fig. 5 of the main text. Beyond the critical field, $B_{\parallel} > B_{cr}$, the spins of the eigenstates do not complete a full rotation going around the Fermi contours. Furthermore, the out-of-plane magnetic field B_z opens a gap at the Dirac point, leading to a non-zero $J^{(2)}$ for $B_{\parallel} < B_{cr}$. In light of these observations, it is an interesting question whether our results could be related to topological properties of the energy bands.

E. Scattering time approximation, temperature, and gate-voltage

In our calculations, we assumed a single relaxation time τ . Furthermore, we assumed that the second-order current is characterized by τ^2 , leading to γ being independent of τ . As can be seen in the above calculations, and as demonstrated by Ideue *et al.* [1], even within this approximation, γ should change with temperature and carrier density. However, in our system, the dependence of γ on these parameters is too strong for the relatively small variations of temperature and gate-voltage (even when accounting for both the change in μ and in λ caused by the gate). A similar strong dependence of γ on temperature was previously observed in SrTiO₃ [3]. In that work, He *et al.* speculated that the assumption that the spin states are well-defined may be inaccurate and that coherent superpositions of spin states could substantially change the calculations. We also observe a strong dependence on gate-voltage, and note that as shown previously for the (111) LaAlO₃/SrTiO₃ interface [4], the spin-relaxation becomes dominated by a D'yakonov-Perel' type mechanism at negative gates, resulting in incoherent spin-orbit scattering effects on transport. While it would be interesting to incorporate such effects into the calculations, such an analysis is beyond the scope of this work. We do however note that for a given temperature and gate-voltage, our minimal model is sufficient to explain the critical in-plane magnetic field, and the strong effect of the out-of-plane field.

F. Effects of a presumed second band

For simplicity of our theoretical arguments we assume a single-band model. This assumption is strongly supported by the linear Hall measurements shown in Fig. 1(a) of the main text; a second band would manifest itself by deviations from linearity, which are not detectable in our data. Yet, one could argue that a second band exists, occupied by an electron density which is much smaller than the electron density in the first band. This would result in an additional contribution to the second harmonic current, given by Eq. (3) of the main text, with the corresponding Fermi-Dirac distributions and energy bands,

$$J_2^{(2)} = -e^3 \tau^2 E^2 \sum_{r=\pm} \int \frac{dk_x dk_y}{(2\pi)^2} \frac{\partial^3 \varepsilon_{k,2}^r}{\partial k_x^3} f_0^r(\varepsilon_{k,2}, \tilde{\mu}_2), \quad (\text{S17})$$

where $\tilde{\mu}_2$ is the chemical potential measured from the bottom of the second band. One could then suspect that $J_2^{(2)}$ is a non-negligible contribution to the second harmonic current; in fact, if the first band is fully symmetric, its contribution to the second harmonic current vanishes, and $J_2^{(2)}$ would be the only contribution. The critical field observed in the experiment could then be suspected as a result of a transition in the structure of the Fermi contours of the second band, and not the first band.

We now show that all such transitions for a possible low-population second band either occur at magnetic fields far below the critical field H_{cr} observed in the experiment, or do not entail a sharp increase in the second harmonic current. In the following, for the simplicity of the discussion, we assume that the effective mass and the spin-orbit interaction of the second band are the same as those of the first band (few meV for the spin-orbit energy and few m_e for the electron mass, these are typical for the (111) LaAlO₃/SrTiO₃ interface [5], see also Fig. S6). In the absence of a magnetic field, the bottom of the spin-polarized bands lies at $\varepsilon = -m\lambda^2/2$, and the Dirac point of the second band is at $\varepsilon = 0$. Since $\tilde{\mu}_2$ can be arbitrarily small, it is important to distinguish between three scenarios:

1. $\tilde{\mu}_2 < m\lambda^2/2$. At fields $|B_y| < \tilde{\mu}_2$, both spin-polarized bands are occupied, but the Dirac point of the second band is excluded from the Fermi contours. In this region, one finds $J_2^{(2)} \sim B_y$, as shown in Ref. [1]. One of the spin-polarized bands becomes fully depleted at $|B_y| > \tilde{\mu}_2$, and one could suspect that a drastic change in the dependence of $J_2^{(2)}$ on B_y occurs at $B_{cr,2} = \tilde{\mu}_2 < m\lambda^2/2$; yet, using typical values for m and λ , we find that this new critical field would be very small, several orders of magnitude smaller than the observed H_{cr} .
2. $m\lambda^2/2 < \tilde{\mu}_2 < m\lambda^2$. Similar to the previous case, a transition occurs at $|B_y| = \tilde{\mu}_2 < m\lambda^2$, which results in a field much smaller than that observed in our experiment. It should be noted that there is another transition in this case, which occurs at an even smaller field $|B_y| = \sqrt{2m\lambda^2(\tilde{\mu}_2 - m\lambda^2/2)}$. Below this field the Dirac point is included in the Fermi contours, so that $J_2^{(2)}$ vanishes, while above it (and below $\tilde{\mu}_2$) we have $J_2^{(2)} \sim B_y$, as stated above. This transition occurs at a field smaller than the transition at $\tilde{\mu}_2$ mentioned above, and anyway does not lead to a sharp increase in $J_2^{(2)}$.
3. $m\lambda^2 < \tilde{\mu}_2$. This case reproduces the scenario considered in the main text for the primary band; both spin-polarized bands are occupied, the Dirac point of the second band is included in the Fermi contours at small magnetic fields, and $J_2^{(2)}$ vanishes, until a critical field $B_{cr,2} = \sqrt{2m\lambda^2(\tilde{\mu}_2 - m\lambda^2/2)}$ is reached. Since the Hall measurement implies that the occupation of the second band (if it exists) is smaller by several orders of magnitude than the occupation of the first band (and thus the same holds for the chemical potentials measured from the bottom of the bands), we expect to observe a critical field well below H_{cr} measured in the experiment. At higher magnetic fields, another transition occurs at $|B_y| = \tilde{\mu}_2$, once one of the spin-polarized bands becomes fully depleted. Assuming that $\tilde{\mu}_2$ is smaller than $\tilde{\mu}_1$ by 2 or 3 order of magnitude, this transition point could in fact lie within the same order of magnitude as the observed H_{cr} . Yet, one could check that this transition does not entail a sharp increase in $J_2^{(2)}$, but rather there is a smooth transition in $J_2^{(2)}$, and it keeps decaying as $\sim 1/B_y^3$, similarly to Eq. (S14).

We therefore conclude that all possible transitions in the structure of the Fermi surface that are associated with a presumed second-band either occur at magnetic fields far below the observed H_{cr} , or are not accompanied by a sharp increase in the second harmonic current.

II. SUPPLEMENTARY SECTION 2 — ADDITIONAL MEASUREMENTS:

In this section, we provide supplemental magneto-transport measurements. In Fig. S2 and Fig. S3, we present measurements conducted on several devices with current driven along various crystal axes. The remainder of the figures in this supplemental document presents various magneto-transport measurements conducted on the same device shown in the main text.

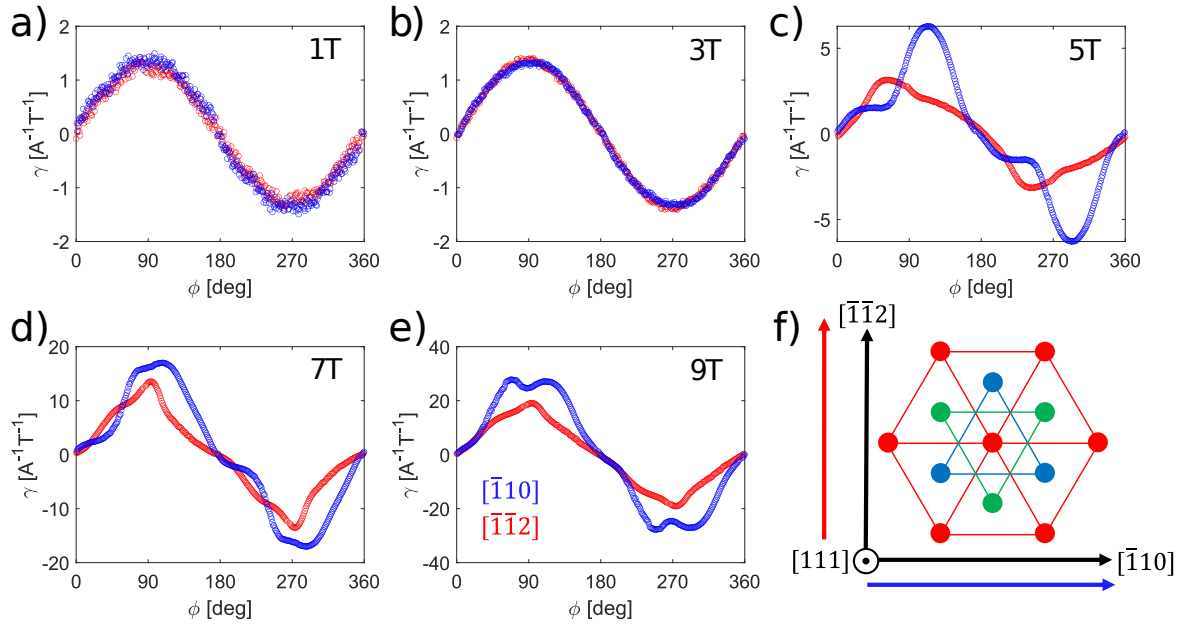


FIG. S2. Non-linear transport coefficient γ versus ϕ for two Hall bar devices patterned along different crystal axes subjected to various in-plane magnetic fields. Data in blue/red corresponds to devices with current running along the $[\bar{1}10]$ / $[\bar{1}\bar{1}2]$ axis. ϕ is defined as the angle between the current and the magnetic field. (a)-(e) Shows data for various magnitudes of the magnetic field from 1 T to 9 T. (f) Sketch of the $[111]$ face of the Ti atoms in the SrTiO_3 crystal. Different colors of the atoms correspond to different locations along the $[111]$ axis. Blue/red arrows mark the direction of current for the data shown here. Data shown in blue ($I \parallel [\bar{1}10]$) corresponds to the device shown in the main text. Measured at $T=3$ K and $R_s=380 \Omega$ for the $[\bar{1}10]$ device, and $R_s=404 \Omega$ for the $[\bar{1}\bar{1}2]$ device.

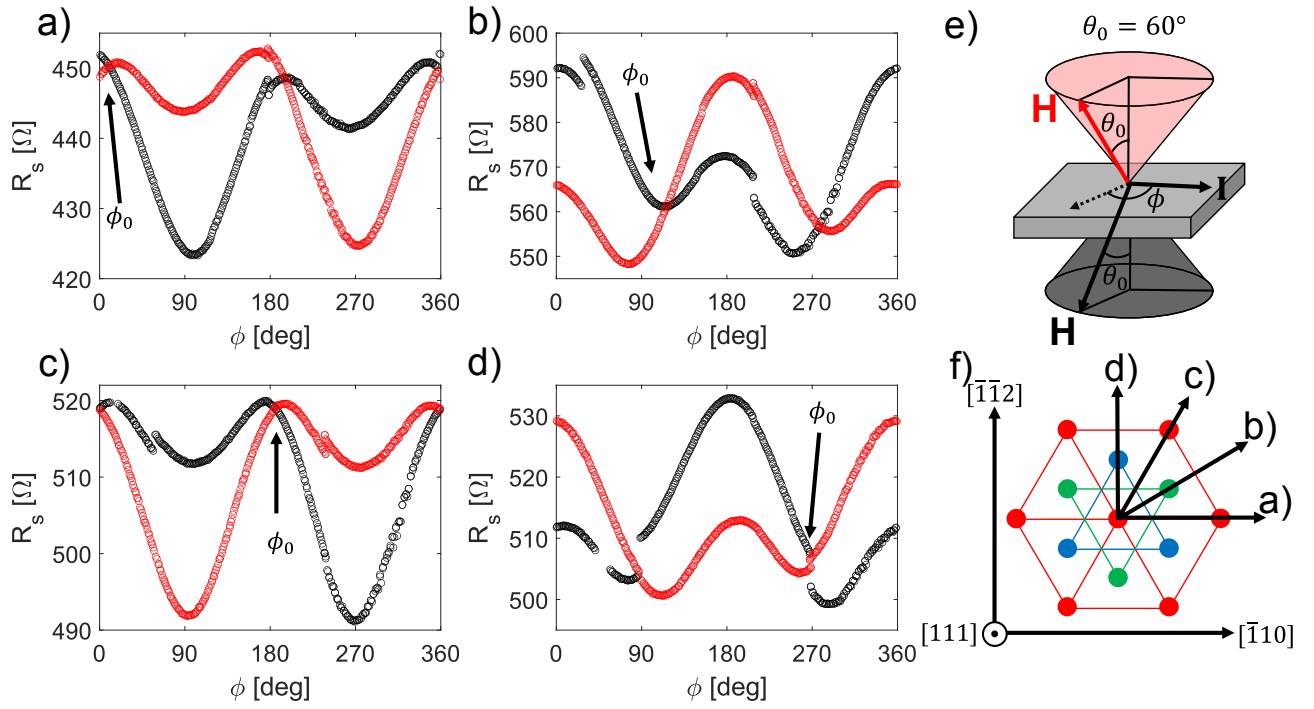


FIG. S3. Resistance versus in-plane magnetic field angle ϕ while keeping a constant positive/negative out-of-plane magnetic field is shown in red/black. (a)-(d) Measurements are shown for four different devices where current is driven along different crystal axes. (e) Sketch of magnetic field orientation. (f) Sketch of the [111] face of the crystal, showing the direction of current in (a)-(d). The angle ϕ_0 , defined as the angle where both curves intersect (see also main text), rotates by 90° whenever the current is rotated by 30° , reflecting the three-fold symmetry of the [111] face. In-plane magnetic field is always 7.8 T, while out-of-plane field is 4.5 T (red) and -4.5 T (black). $T=1.9$ K, and R_s for various devices are: (a) 474 Ω , (b) 608 Ω , (c) 541 Ω , (d) 531 Ω . Resistances here vary more significantly from rest of figures since no gate-voltage was applied.

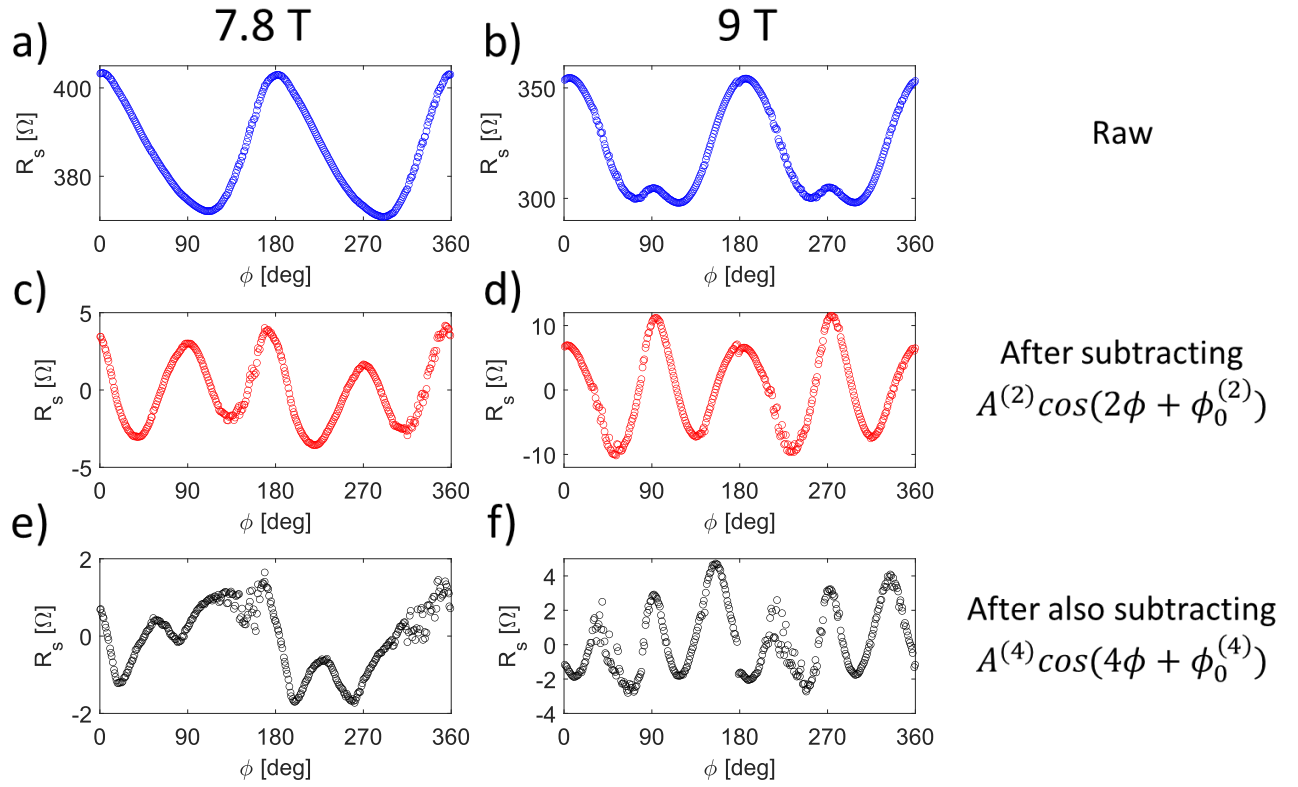


FIG. S4. In-plane first-harmonic magnetoresistance measurements for the device shown in the main text. (a)-(b) Raw data of resistance versus in-plane magnetic field angle for magnetic field magnitudes of 7.8 T and 9 T. A mostly two-fold dependence on ϕ is observed. (c)-(d) Data after subtracting two-fold component (via Fourier), revealing a mostly four-fold behavior. (e)-(f) After also subtracting the four-fold component, a six-fold behavior can be seen. The effect is larger and hence can be observed more clearly at 9 T. Data taken from device shown in main text. 9 T measurement set conducted at $T=3$ K and $R_s=380$ Ω , 7.8 T measurements at $T=2$ K and $R_s=407$ Ω

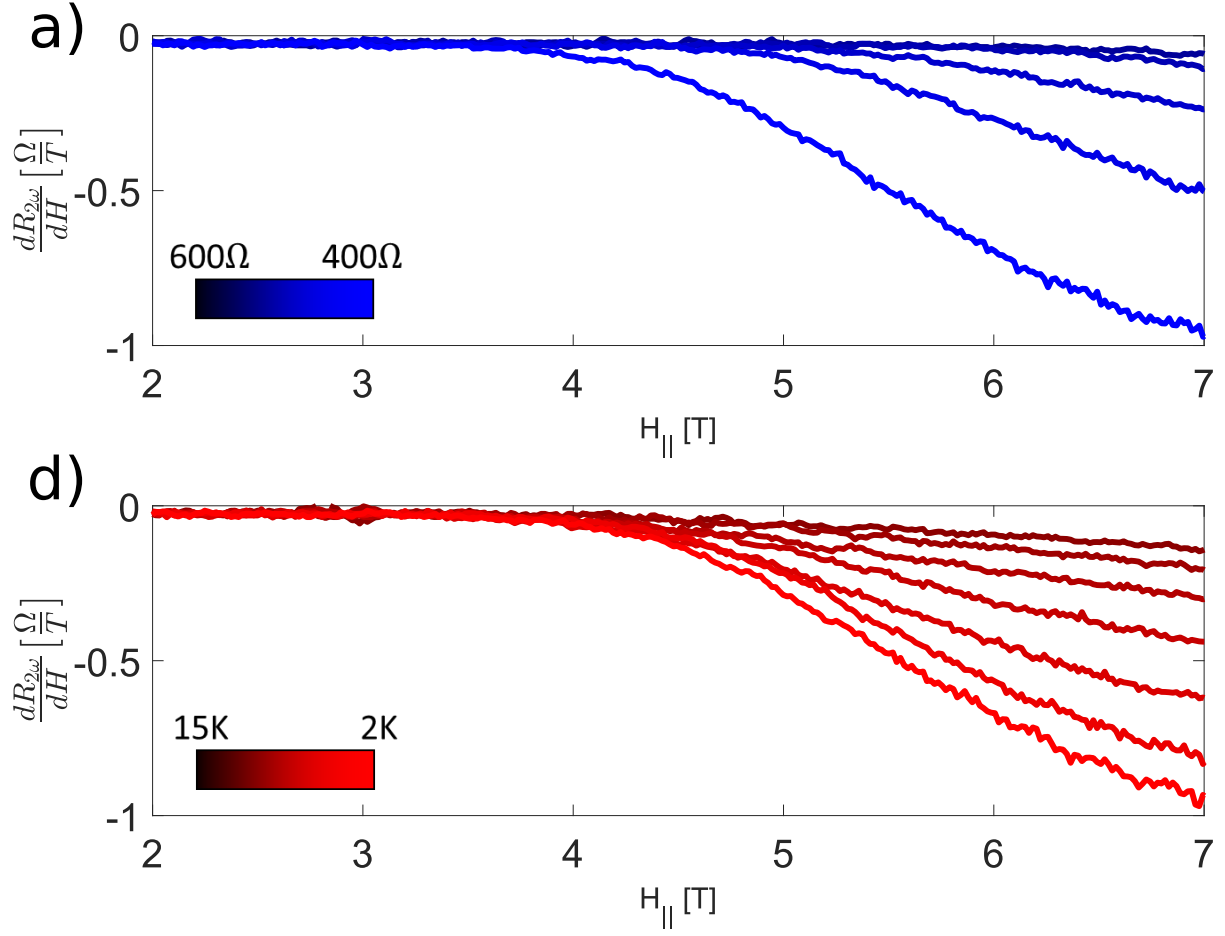


FIG. S5. Derivative of $R_{2\omega}$ with respect to the magnetic field for various gates (a) and temperatures (b). Data corresponds to measurement shown in main text. By examining the derivative, a clear change in the critical magnetic field can be observed for different gates, while temperature mostly reduces the magnitude of the effect but does not change H_{cr} .

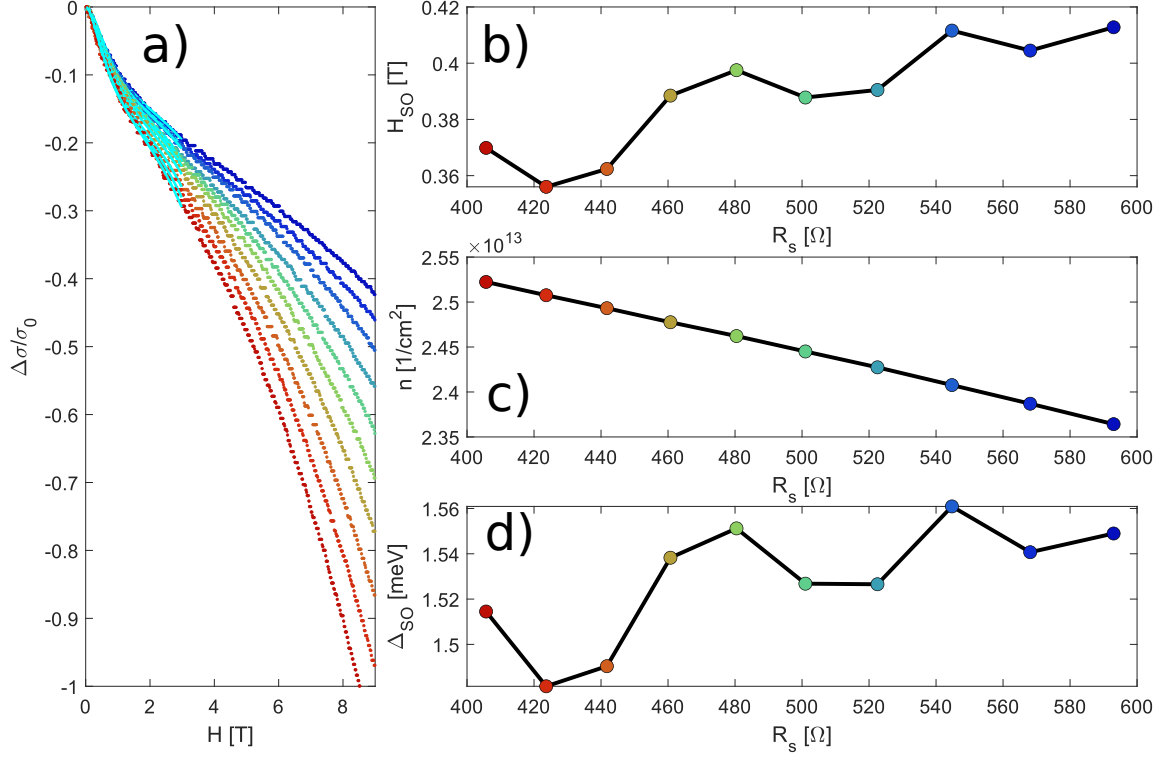


FIG. S6. (a) Weak anti-localization measurements presented as change in conductivity divided by the quantum conductance as function of perpendicular magnetic field. Cyan lines correspond Hikami-Larkin-Nagaoka fit for diffusive two-dimensional electrons with negligible Zeeman splitting (see Lesne *et al.* for similar analysis [5]). Different colors correspond to different gate voltages. (b) Spin-orbit field H_{SO} extracted from the fits shown in (a) for various gate-voltages (see x-axis for corresponding sheet resistance of every measurement). (c) Two-dimensional electron density extracted from Hall measurements. (d) Spin-orbit energy Δ_{SO} calculated using (b), (c), and taking an effective mass of $3m_e$. Measurements conducted at 2 K. The contribution of the Hall resistance to σ was neglected.

III. SUPPLEMENTARY SECTION 3 — EFFECT OF IN-PLANE MAGNETIC FIELD ON THE HALL EFFECT:

The Hall effect shown in the main text only contains a perpendicular magnetic field and shows a perfect linear behavior. However, a planar magnetic field was previously shown to contribute to the Hall signal in two distinct ways in the $\text{LaAlO}_3/\text{SrTiO}_3$ interface. In this section we demonstrate that these effects are also observed in the (111) $\text{LaTiO}_3/\text{SrTiO}_3$ interface studied here.

In Fig. S7 we show the anomalous planar Hall effect for various gate-voltages. This is a Hall contribution appearing even when the magnetic field is completely in the plane of the interface. A linear low-field slope can be observed followed by an anomalous contribution beyond some critical in-plane field. As the gate-voltage becomes more negative (higher resistance), the anomalous planar behavior is not observed. Similar effects were recently observed in the (111) $\text{LaAlO}_3/\text{SrTiO}_3$ interface and related to the formation of Berry curvature dipoles [5]. In that system, this behavior was reported only once a two-band behavior was observed in the normal Hall signal. However, in the interface studied here, this planar Hall effect appears despite the presence of only one electronic band. It is important to note that results were antisymmetrized with respect to the magnetic field to prevent contributions from the symmetric planar Hall effect which originates from anisotropic magnetoresistance.

We also note that we can confirm that the low-field linear slope is real and is not a result of a misalignment artifact. We are able to confidently make this claim since these measurements were conducted in a dilution refrigerator with a vector magnet. Prior to the planar Hall measurements, the sample was brought exactly to its superconducting critical temperature (defined as half the normal-state resistance) under the presence of a 1 T in-plane magnetic field. Then, a small out-of-plane magnetic field was applied and varied slowly. We show the results of longitudinal resistance in the

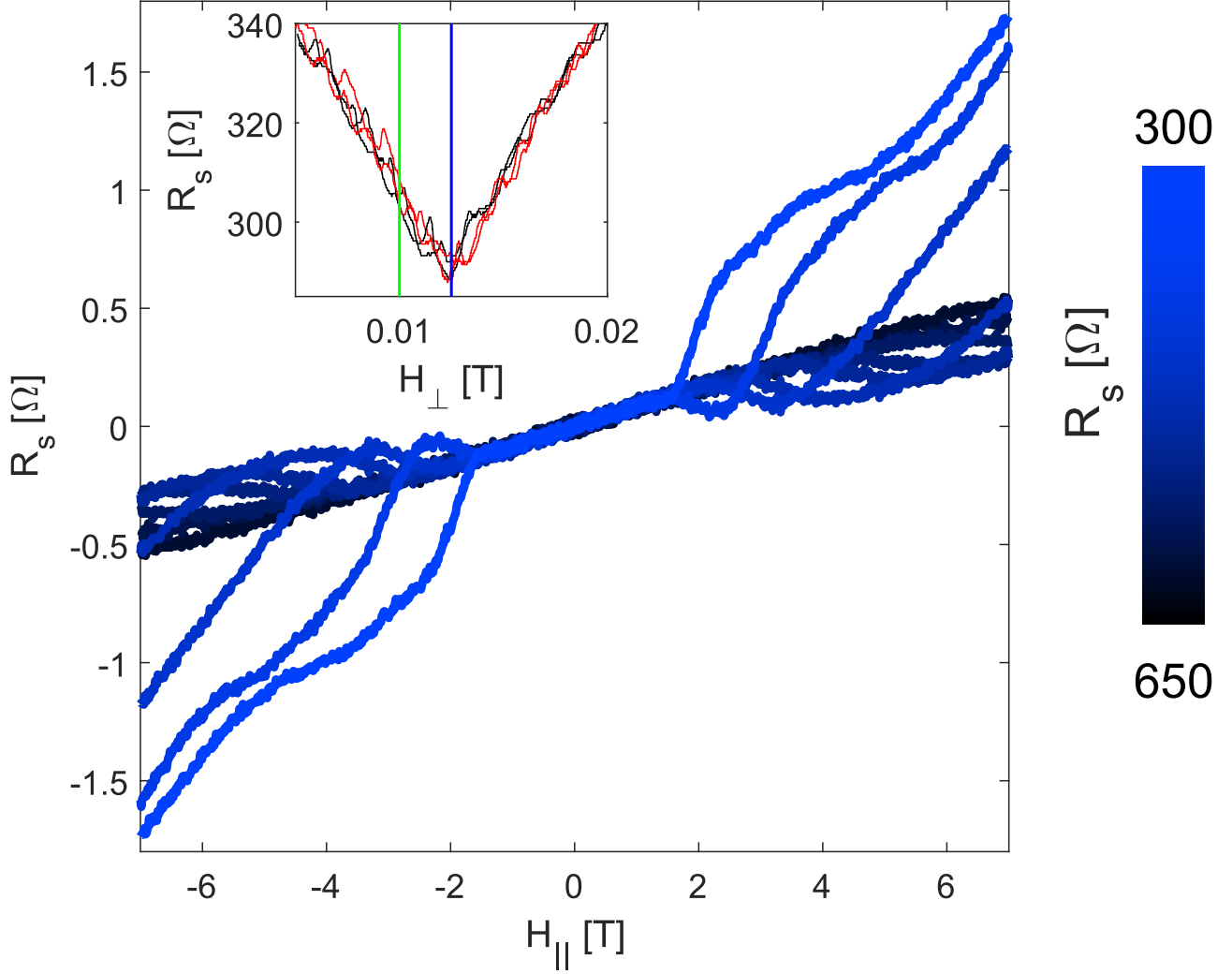


FIG. S7. Anomalous planar Hall effect. We show the results of the the antisymmetric Hall effect at $T=0.7$ K when the magnetic field is completely in the plane of the interface. A linear slope is seen followed by an anomalous planar contribution. Inset: Alignment measurements explained in the text of this section.

inset of Fig. S7 where a clear minimum of resistance can be seen. Since the superconductivity is much more sensitive to an out-of-plane magnetic field, the system will be closest to the superconducting state (lower resistance) when the magnetic field is exactly in the plane of the interface. Therefore, we can use this measurement to accurately account for the misalignment of our sample and the measurements shown here and in the following figure are corrected for this misalignment. To further illustrate this point, we mark in the inset the amount of misalignment field needed to explain the linear slope from a normal Hall effect contribution through misalignment (green line). As can be seen, our accuracy is much better than this amount of misalignment. This alignment measurement was repeated four times with varying sweep directions (black/red) to account for thermal fluctuations.

When both in-plane and out-of-plane magnetic fields are applied, a different contribution to the Hall effect is measured. We show this in Fig. S8 (a), where a constant magnetic field of 7 T is applied in the plane of the interface and an out-of-plane magnetic field is changed. It can be seen that for more negative gate voltages (high R_s), the Hall effect is linear with the out-of-plane field, meaning the it is unaffected by the presence of the in-plane field. However, for more positive gate voltages, an anomalous contribution to the Hall effect can be observed. This anomalous Hall effect was previously observed in the $\text{LaAlO}_3/\text{SrTiO}_3$ interface [6, 7]. As noted in the main text, these effects were only observed along with a two-band Hall effect, while in our interface they appear with a single occupied band.

In Fig. S8 (b), we apply a constant out-of-plane field while changing the in-plane magnetic field. We then plot the measured Hall resistance after subtracting the Hall resistance for zero-in-plane magnetic field. The resulting resistance

is the anomalous contribution to the Hall effect from the in-plane magnetic field. In the inset of this figure, we show the anomalous contribution for $H_{\parallel}=7$ T, $H_{\perp}=0.3$ T versus the sheet-resistance (gate-voltage). It can be seen that the anomalous contribution decays when the sheet resistance is larger (more negative gate-voltage). The appearance of these effects only when a large in-plane magnetic field and a positive gate-voltage are applied leads us to speculate that they are also related to the exclusion of the Dirac point from the Fermi contour and the related change to the Fermi contour and spin texture.

We note that these measurements were antisymmetrized with respect to the total field,

$$R_{xy}(H_{\parallel}, H_{\perp}) = \frac{R_{xy}(H_{\parallel}, H_{\perp}) - R_{xy}(-H_{\parallel}, -H_{\perp})}{2}. \quad (\text{S18})$$

The Hall resistance was then antisymmetrized again with respect to H_{\perp} to remove the contribution of the anomalous planar Hall effect shown in Fig. S7.

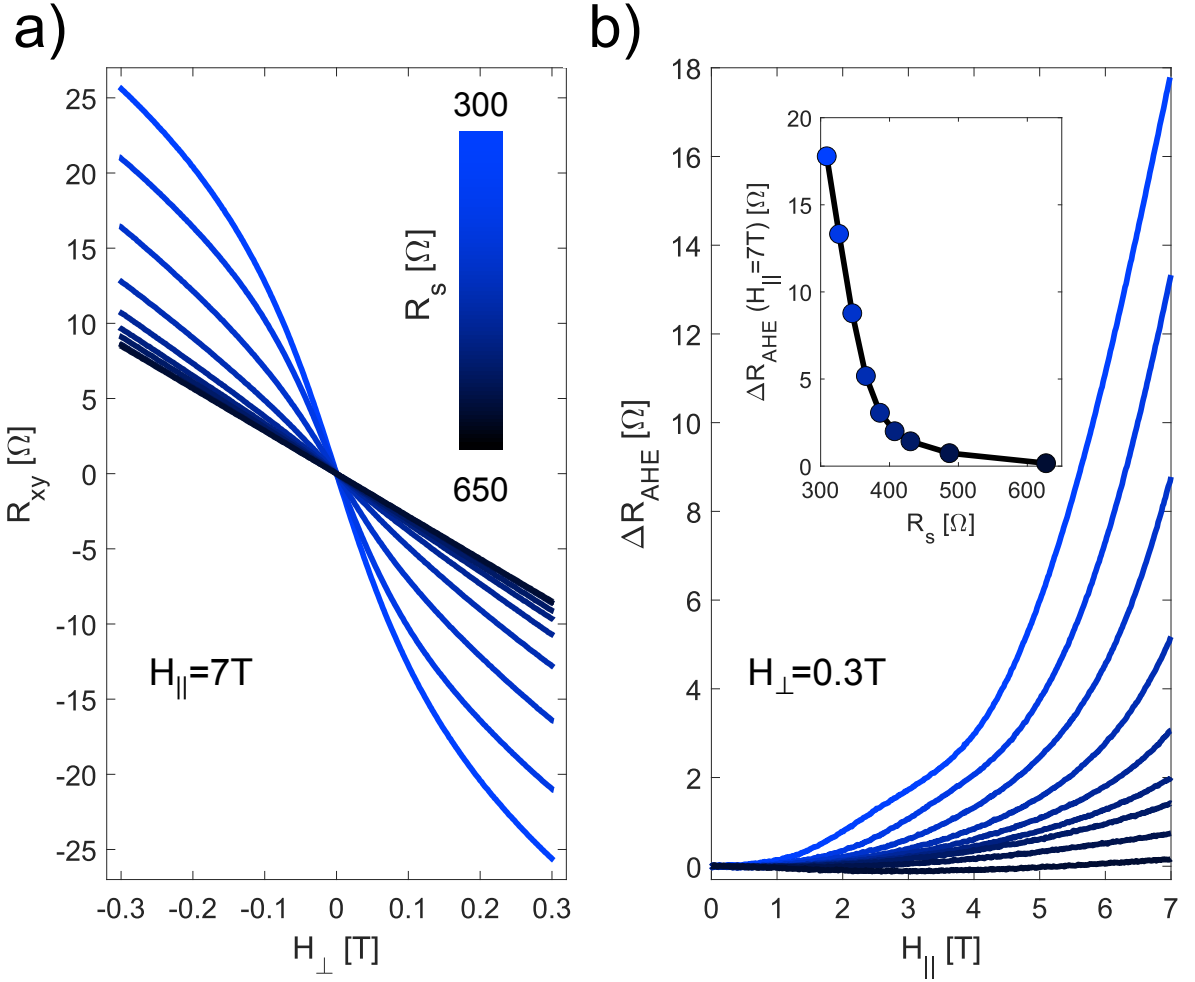


FIG. S8. Constant in-plane magnetic field drives anomalous Hall behavior. (a) A constant in-plane magnetic field of 7 T is kept while the out of plane magnetic field is swept shown for various gate voltages. To remove contributions of the planar Hall effect, each magnetic field sweep is repeated with -7 T and the data is antisymmetrized with respect to the total magnetic field. To remove contributions from the anomalous planar Hall effect (which is antisymmetric with the in-plane field, see previous figure) the results are antisymmetrized again with respect to the perpendicular magnetic field. As the gate-voltage becomes more positive (lower resistance), the anomalous contribution to the Hall effect increases. (b) Similar to the analysis done in (a), but the out-of-plane magnetic field was constant at 0.3 T, while the in-plane magnetic field was swept. The normal Hall resistance (no in-plane field) was subtracted from all the measurements to show the anomalous component. Inset: anomalous contribution for $H_{\parallel}=7$ T, $H_{\perp}=0.3$ T versus the sheet-resistance (gate-voltage). All measurements conducted at $T=0.7$ K.

IV. SUPPLEMENTARY SECTION 4 — SAMPLE PREPARATION, EXPERIMENTAL METHODS:

22 mono-layers of LaTiO_3 were grown with the use of the Pulsed Laser Deposition (PLD) technique at a partial pressure of oxygen of 1×10^{-4} Torr, a temperature of 780°C , and energy density of $1.15 \frac{1}{\text{cm}^2}$. The layers were deposited on atomically flat, 0.5 mm thick (111) SrTiO_3 substrates. After deposition, the samples were annealed at 400°C and a pressure of 200 mTorr for 1 hour. The sample was then cooled to room temperature, and while still in the growth chamber, an 8.5 nm thick amorphous BaTiO_3 capping layer was deposited to prevent oxidation of LaTiO_3 to $\text{LaTiO}_{3+\delta}$. This capping layer was grown at a partial pressure of oxygen of 1.5×10^{-3} Torr. The first 60 pulses were grown at a rate of 1 Hz, while the rest was grown at 3 Hz. The lithography-defined current paths along different crystallographic axes were defined with the use of an amorphous material hard mask (see Ref. [8] for details).

Back-gate electrodes were attached to the bottom of the SrTiO_3 substrates with Ag paint. Angle-dependence magneto-transport measurements were conducted using a two-axis piezo rotator in an Attocube attoDRY2100 system with a maximal magnetic field of 9 T. Hall measurements up to 14 T were conducted in a Quantum Design Physical Property Measurement System (PPMS). Superconductivity measurements were conducted in a Oxford Instruments Triton dilution refrigerator with a base temperature of 20 mK and a (8 T, 1 T, 1 T) vector magnet. Measurements throughout this work were conducted in different instruments and cool-downs, resulting in slight variations of sheet resistances and base temperatures in different measurements. Second-harmonic transport measurements were conducted by driving an alternating current with an amplitude of $100 \mu\text{A}$ and frequency of 17.321 Hz using a Keithley 6221 current source. This current amplitude was chosen to provide a clear signal while not damaging the samples. In Fig. S9 we demonstrate that γ is independent of the current magnitude, or more simply, that $V \sim I^2$. The relatively low frequency was chosen to prevent the effects of parasitic capacitance contributions. A trigger link was connected from the current source to a Stanford Research Systems SR830 lock-in, set to measure the second harmonic with a $-\frac{\pi}{2}$ phase. To account for the slight out-of-plane wobble of the sample while rotating the in-plane angle ϕ , the out-of-plane angle θ changed along with ϕ to remain perfectly in-plane. The exact θ corresponding to the in-plane orientation was calibrated for several ϕ angles prior to the measurement by measuring the sharp in-plane peak seen in the second-harmonic transport (as seen in Fig. 3(a)).

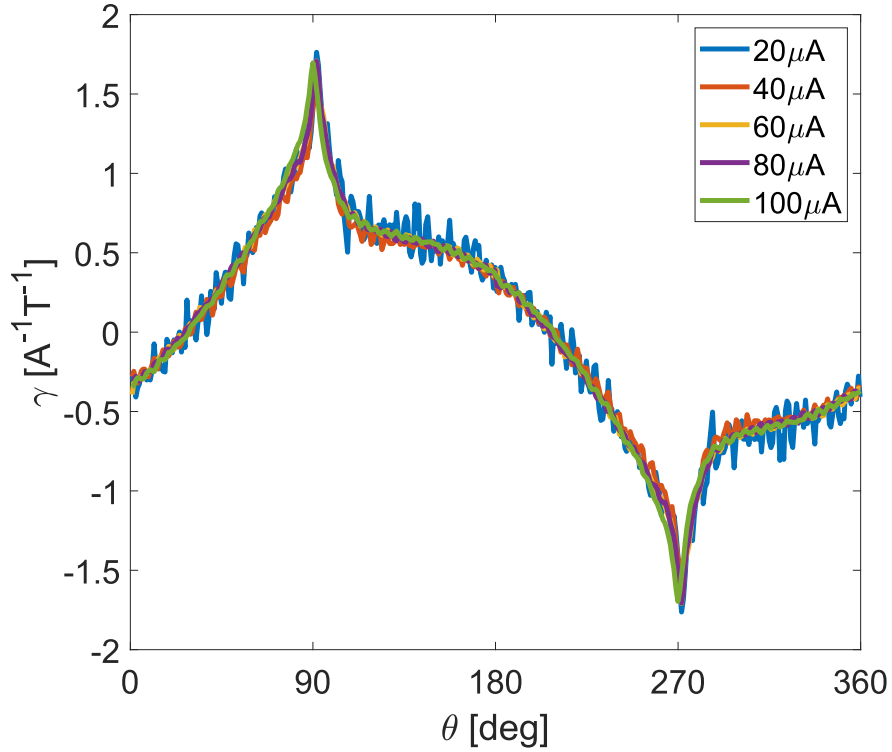


FIG. S9. γ , which is proportional to $\frac{V}{I^2}$, versus out-of-plane angle of magnetic field for various driving current amplitudes. It can be observed that γ does not depend on the current amplitude, or more simply, that $V \sim I^2$. All measurements conducted at $|\mathbf{H}|=10 \text{ T}$, $T=10 \text{ K}$, $R_s=420 \Omega$, in the transverse field orientation (at depicted in the top panel of Fig. 3 (e) in the main text).

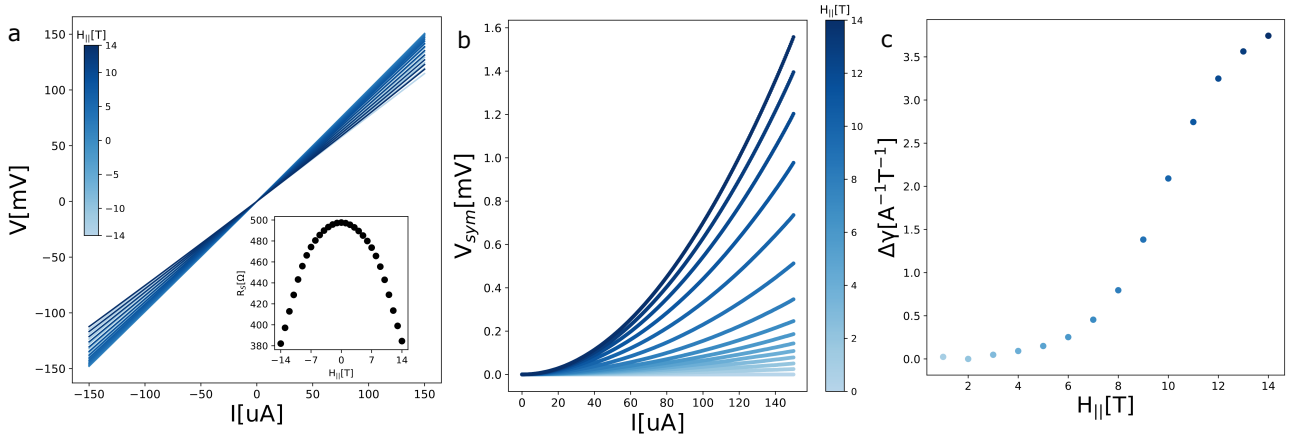


FIG. S10. DC measurements: (a) Raw voltage versus current curves at different transverse magnetic field values. Inset: linear sheet resistance at the different magnetic fields. The device length to width ratio was 2 and therefore there is a factor of 2 between the raw voltage-current curves and the sheet resistance. (b) Symmetrizing the voltage-current curves with respect to the current at different magnetic fields. This component is the non-linear voltage. (c) Non-linear γ factor extracted by parabolic fitting of (b), see main text for the definition of γ . Note that measurements were antisymmetrized with respect to the magnetic field, similar to results presented in the main text. These measurements show that the non-linear enhancement effect seen in Fig. 2 of the main text is reproduced when direct current is applied instead of applying alternating current and performing second-harmonic voltage measurements. Measurements taken at $T = 6\text{K}$ and $R_s = 497.5 \Omega$.

-
- [1] T. Ideue, K. Hamamoto, S. Koshikawa, M. Ezawa, S. Shimizu, Y. Kaneko, Y. Tokura, N. Nagaosa, and Y. Iwasa, *Nature Physics* **13**, 578 (2017).
- [2] R. Battilomo, N. Scopigno, and C. Ortix, *Phys. Rev. Res.* **3**, L012006 (2021).
- [3] P. He, S. M. Walker, S. S.-L. Zhang, F. Y. Bruno, M. S. Bahramy, J. M. Lee, R. Ramaswamy, K. Cai, O. Heinonen, G. Vignale, F. Baumberger, and H. Yang, *Phys. Rev. Lett.* **120**, 266802 (2018).
- [4] P. K. Rout, E. Maniv, and Y. Dagan, *Phys. Rev. Lett.* **119**, 237002 (2017).
- [5] E. Lesne, Y. G. Sağlam, R. Battilomo, M. T. Mercaldo, T. C. van Thiel, U. Filippozzi, C. Noce, M. Cuoco, G. A. Steele, C. Ortix, and A. D. Caviglia, *Nature Materials* **22**, 576 (2023).
- [6] M. Ben Shalom, M. Sachs, D. Rakhmilevitch, A. Palevski, and Y. Dagan, *Phys. Rev. Lett.* **104**, 126802 (2010).
- [7] A. Joshua, J. Ruhman, S. Pecker, E. Altman, and S. Ilani, *Proceedings of the National Academy of Sciences* **110**, 9633 (2013).
- [8] E. Maniv, M. B. Shalom, A. Ron, M. Mograbi, A. Palevski, M. Goldstein, and Y. Dagan, *Nature Communications* **6**, 8239 (2015).